Journal of *Marine Science and Engineering*

MDPI

Article

Synergistic Effects of Ocean Background and Tropical Cyclone Characteristics on Tropical Cyclone-Induced Sea Surface Cooling in the Western North Pacific

Rao Rao, Chengcheng Yu *, Peng Bai and Bo Li

Marine Science and Technology College, Zhejiang Ocean University, Zhoushan 316022, China; raorao@zjou.edu.cn (R.R.); pengbai@zjou.edu.cn (P.B.); acelibo@zjou.edu.cn (B.L.)
* Correspondence: yuchengcheng@zjou.edu.cn

Abstract: Tropical cyclones (TCs) induce intense mixing in the upper ocean, which significantly impacts sea surface temperature (SST) and marine environment. Previous studies have shown that TCs can cause a decrease in sea surface temperature (DSST), while further research is required to elucidate the factors influencing SST changes. This study employs satellite observations and reanalysis data from the western North Pacific during 2002–2020 to investigate the relationship between DSST and the ocean background state (BG). In addition, by incorporating TC characteristics, we construct indices to explore the synergistic effects of TCs and BG on DSST, enabling a more comprehensive understanding of the mechanisms governing DSST variability. The results indicate that DSST exhibits significant monthly variations, with the maximum DSST in September for coastal regions and in August for offshore regions. Regardless of TC characteristics, when the mixed layer depth (MLD) exceeds 60 m or thermocline depth (TD) exceeds 115 m, it is difficult for the DSST to exceed 1 °C. In both coastal and offshore regions, MLD and TD exhibit moderate negative correlations with DSST, with values around −0.3. When TC characteristics are incorporated, these correlations rise to approximately 0.6, highlighting the importance of jointly considering BG and TC effects in characterizing DSST. The findings of this study provide theoretical support for improving the capability to predict DSST changes before the TC approaches the coast.

Keywords: Western North Pacific; tropical cyclones; sea surface cooling; ocean background state

check for updates

Academic Editor: Anatoly Gusev

Received: 14 April 2025
Revised: 3 May 2025
Accepted: 12 May 2025
Published: 14 May 2025

Citation: Rao, R.; Yu, C.; Bai, P.; Li, B. Synergistic Effects of Ocean Background and Tropical Cyclone Characteristics on Tropical Cyclone-Induced Sea Surface Cooling in the Western North Pacific. *J. Mar. Sci. Eng.* **2025**, *13*, 955. https://doi.org/10.3390/jmse13050955

Copyright: © 2025 by the authors. Licensee MDPI, Basel, Switzerland. This article is an open access article distributed under the terms and conditions of the Creative Commons Attribution (CC BY) license (https://creativecommons.org/licenses/by/4.0/).

1. Introduction

Tropical cyclones (TCs) are frequent natural hazards in the Western North Pacific (WNP) during the summer [1], causing widespread destruction in coastal regions through intense winds and large waves [2]. TCs are closely coupled with oceanic conditions, exhibiting strong interactions [3–6]. A sea surface temperature (SST) above 26 °C provides the energy required for TC intensification [7–9], and SST largely determines the maximum potential intensity a TC can reach. Conversely, stronger TCs induce a greater decrease in sea surface temperature (DSST) along their tracks [1,10–12]. In addition to TCs, the ocean background state (BG) can also affect DSST; therefore, studying the synergistic effects of TCs and BG on DSST is essential [13–18]. Furthermore, since coastal and offshore regions exhibit different ocean structures, it is necessary to investigate DSST in each region separately.

During the passage period of TCs, DSST is primarily driven by dynamic processes, including strong wind-driven vertical mixing of cold subsurface water and upwelling [19–23].

In offshore regions, vertical mixing plays a dominant role, whereas in coastal regions, advection processes play a primary role [24,25]. In contrast, thermal processes such as heat exchange contribute less than 20% to DSST [26–28]. The dynamic and thermal factors inducing DSST are both influenced by the TCs and BG characteristics. For instance, slow-moving, intense TCs generally cause greater DSST than fast-moving, weaker TCs [29–34]. Additionally, Pun et al. [32] demonstrated that when TCs curve northward along their tracks, both TC size and the average radius of maximum wind increase significantly, thereby sustaining the intensity of DSST. Previous studies have emphasized the importance of TC characteristics in influencing DSST. For example, Pun et al. [35] reported moderate correlations between DSST and parameters such as TC size, intensity, and translation speed. Vincent et al. [12] proposed the Wind Power Index to quantify DSST based on TC forcing, while Cui et al. [36] applied machine learning to identify intensity, size, and speed as key predictors. In addition to TC characteristics, the upper ocean vertical structure also plays a key role in TC-induced mixing [37].

Since vertical mixing depends strongly on the vertical temperature structure, the degree of DSST is closely linked to pre-existing stratification [11,38]. Moreover, when TCs are weaker, faster-moving, or smaller, they induce less intense and shallower mixing, allowing the stratified temperature profile to exert an increasingly dominant influence on DSST [35,39–44]. Mixed layer depth (MLD) and thermocline depth (TD) are key indicators of the vertical temperature profile. MLD refers to the depth of the upper ocean layer with relatively uniform temperature and salinity, while TD represents the depth at which the ocean temperature decreases most rapidly with depth. Previous studies have indicated that shallow MLD and TD facilitate the entrainment of colder subsurface waters by wind-driven mixing and upwelling, resulting in a significant DSST. Conversely, when the entrainment is limited, DSST is substantially suppressed [45–50]. Furthermore, freshwater enhances the ocean's salinity stratification, which fosters the formation of a barrier layer at the base of the mixed layer. When TCs pass through the barrier layer region, this layer suppresses the vertical mixing and DSST induced by TCs [51–53]. Moreover, research by Miles et al. [54] shows that the suppression of DSST can reach up to 57%. Additionally, in the Bay of Bengal, the DSST during the pre-monsoon season is approximately three times that after the monsoon season. This difference is essentially related to seasonal changes in oceanic stratification rather than to differences in TC wind energy input. During the post-monsoon season, stronger thermal stratification and significant upper-ocean freshening strongly inhibit DSST induced by vertical mixing beneath TCs. On average, thermal stratification contributes to 60% of this cooling reduction during postmonsoon season, while haline stratification contributes to the remaining 40% [55,56]. Previous studies have highlighted the role of ocean background conditions in DSST. For instance, Da et al. [24] and Vincent et al. [56] demonstrated the importance of stratification metrics like MLD and SST–T100, while Oey [57] proposed a nonlinear model capturing upper-ocean structure. However, these parameters are often examined in isolation from TC characteristics, limiting an integrated understanding.

Many studies have investigated TC-induced DSST in both coastal and offshore regions. Observational and numerical simulation research has revealed significant differences in the characteristics of BG between these areas, resulting in distinct oceanic responses to TCs [15,17,25,33,58]. To further explore how the distinct structural characteristics of coastal and offshore regions influence TC-induced DSST, this study divided the WNP into these two regions to examine the spatial and temporal distribution of the BG and DSST, as well as their correlation, and further explore the synergistic effects of the TC and BG on DSST, proposing indices to better characterize DSST. This study provides an understanding of TC-induced ocean cooling, offering both new perspectives on ocean–atmosphere interactions

and a theoretical foundation for improving TC forecasts and early warning systems in coastal regions.

2. Materials and Methods

2.1. Data

TC data are obtained from Version 4 [59] of the International Best Track Archive for Climate Stewardship (IBTrACS), accessed through the NOAA National Centers for Environmental Information. This dataset includes a range of TC characteristic parameters with 3-h temporal resolution, where each interval represents a distinct observation. Hereafter, the term 'observation' refers to a record in the IBTrACS dataset corresponding to a specific 3-h interval. The dataset includes the TCs' geographic coordinates, maximum sustained wind speed (usa_wind in the dataset, MW hereafter for short), translation speed of the TC (storm_speed in the dataset, Trans hereafter for short), radius of 34-knot winds (usa_r34 in the dataset, R34 hereafter for short), and other relevant parameters used to represent the characteristics of TCs. Da et al. [24] demonstrated notable variations in TC and BG within and beyond 500 km from the coastlines. The vertical temperature gradient remains stable in regions within 500 km from the coastline before declining, while the salinity gradient (MLD) decreases (increases) rapidly, and then changes at a slower rate. Beyond 500 km offshore, MW gradually decreases, Trans gradually increases, and R34 remains steady, while these parameters show pronounced variability within 500 km. Building on this finding, this study partitions the WNP into coastal and offshore regions using a 500 km threshold from continental and major island coastlines. Specifically, any TC observations with a distance-to-land (dist2land) value $\leq$ 500 km are classified as coastal regions, while those > 500 km are designated offshore regions.

For the computation of DSST, we use the satellite sea surface temperature dataset (MW_IR), which integrates microwave and infrared remote sensing data provided by Remote Sensing Systems. The spatial resolution of the dataset is 0.25° × 0.25° from June 2002 to now and this daily dataset is less affected by clouds [60].

Subsurface temperature is derived from the GLORYS12V1 [61] reanalysis product (GLOBAL_MULTIYEAR_PHY_001_030), obtained through the Copernicus Marine Environment Monitoring Service (CMEMS). This eddy-resolving dataset provides daily 3D temperature fields from 1993 to present, spanning 50 vertical levels (0–5500 m) with 1/12° horizontal resolution, thus fully meeting the requirements of this study to calculate relevant parameters of the vertical temperature structure in the BG. In addition, previous studies have shown that GLORYS12V1 is consistent with observed ocean temperatures, as it assimilates Argo float data and exhibits good agreement with Argo profiles, with a maximum difference of less than 0.2 °C and a root mean square (RMS) error of 0.02 °C [62]. All data used cover the period from June 2002 to the end of 2020.

2.2. Methods

After the passage of a TC, more than 40% of the DSST recovers to the climatological SST within 5 days [8]. In addition, the average R34 of a TC is approximately 300 km [35], and Yu et al. [63] found that SST decreases were observed at 86% of locations within a 300 km radius from the TC center. Based on these considerations, for each TC observation in this study, DSST is defined as the difference between the SST for the post-TC period (averaged over 1–5 days after the TC) and the pre-TC period (averaged over 1–5 days before the TC). The regional mean SST difference is calculated within a 6° × 6° area centered on the TC location.

For the BG, this study calculates the vertical temperature structure of a 6° × 6° sea area centered on the TC location 5 days prior to the TC. Given that strong TCs typically induce

mixing within the upper 100 m, this study adopts the temperature at 100 m (T100) as a key parameter. It also utilizes temperature difference between the SST and T100, denoted as SST-T100 [56], which effectively captures the extent of DSST associated with upper mixing processes.

To comprehensively explain the effect of the BG on DSST and considering the vertical mixing-induced cooling, this study defines the MLD using a temperature threshold method that captures the vertical temperature structure. A threshold of 0.8 °C is adopted, as it is applicable across global oceans and in all seasons. Compared with other thresholds, 0.8 °C can accurately represent the penetration depth of turbulent mixing [64]. In addition to mixed layer, we also consider the thermocline. To characterize the ocean vertical thermal structure and its influence on DSST, this study adopts thermocline parameters—including thermocline thickness (T Thickness), TD, and thermocline strength (TS)—following the definitions and calculation methods proposed by Fiedler [65]. These parameters provide a physically meaningful description of the thermocline based on established stratification metrics, ensuring consistency with previous studies.

The first parameter, T Thickness is defined as the vertical distance between the thermocline bottom (TB) and MLD:

$$\text{T Thickness} = \text{TB} - \text{MLD} \tag{1}$$

where TB is defined as the depth at which temperature equals the midpoint between the mixed layer temperature (MLT) and T400. T400 is the temperature at 400 m [65]. The region beneath 400 m exhibits a relatively steady vertical temperature gradient largely insensitive to seasonal or regional variability, whereas the MLD shows pronounced seasonal variation. Since the thermocline lies between a seasonally variable upper layer and a relatively stable deep layer, this stratification-based approach provides a consistent and adaptable method for identifying TB across different oceanic regions and seasons.

The second parameter, TD, is defined as the midpoint between the MLD and the TB, approximating the location of the steepest temperature gradient within the thermocline. Compared with previous studies that adopted a fixed isotherm (e.g., 20 °C or 12 °C) to represent thermocline depth, we follow Fiedler's [65] approach by using a location-dependent definition of TD. This method better captures spatial and temporal variability in thermocline structure, and reflects the physical transition zone between the seasonally varying upper ocean and the more stable deep layer. TD is calculated as follows:

$$\text{TD} = (\text{MLD} + \text{TB}) \times 0.5 \tag{2}$$

The third parameter, TS, is defined to quantify the intensity of the thermocline, representing the temperature gradient between the thermocline temperature (TT) and the MLT over the depth range between the TD and MLD, calculated as follows:

$$\text{TS} = \frac{\text{TT} - \text{MLT}}{\text{TD} - \text{MLD}} \tag{3}$$

where MLT represents the temperature at the MLD, and TT is calculated as follows:

$$\text{TT} = \text{MLT} - 0.25 \times (\text{MLT} - \text{T400}) \tag{4}$$

TT is the temperature at the midpoint between MLT and TB temperature, which can be approximated as the temperature at the location of the steepest decline. Equation (4) presents its simplified form.

Six ocean thermal parameters (T100, SST-T100, MLD, T Thickness, TD and TS) are calculated to describe the spatial and temporal differences in the BG and to analyze the impact of the BG on the magnitude of the DSST in the WNP. Additionally, for each TC observation, a $6^\circ \times 6^\circ$ grid was interpolated centered on the TC center. After gridding, only grid cells with at least five TC observations were retained for analysis to ensure statistical robustness. In addition, months with insufficient TC occurrences were excluded from the annual analysis. The main abbreviations used in this study are listed in Table 1.

Table 1. List of abbreviations and their corresponding full terms used throughout this study.

Abbreviation	Full Term	Abbreviation	Full Term
BG	Ocean Background State	TB	Thermocline Bottom
DSST	Decrease in Sea Surface Temperature	TC	Tropical Cyclone
MLD	Mixed Layer Depth	TD	Thermocline Depth
MLT	Mix Layer Temperature	Trans	Translation Speed of TC
MW	Maximum Sustained Wind Speed	TS	Thermocline Strength
R34	Radius of 34-knot Winds	TT	Thermocline Temperature
SST	Sea Surface Temperature	T Thickness	Thermocline Thickness
T100	Temperature at 100 m	WNP	Western North Pacific

Overall, this study uses the GLORYS12V1 dataset to calculate the vertical thermal structure of the BG and the MW_IR dataset to calculate DSST. This study then statistically analyzes the spatiotemporal distributions of BG and DSST. TC characteristics are derived from the IBTrACS dataset to study the synergistic effects of TCs and BG on DSST. Additionally, the distance-to-land from the IBTrACS dataset is used to distinguish between coastal and offshore TCs, with a 500 km threshold from the coastline (Figure 1).

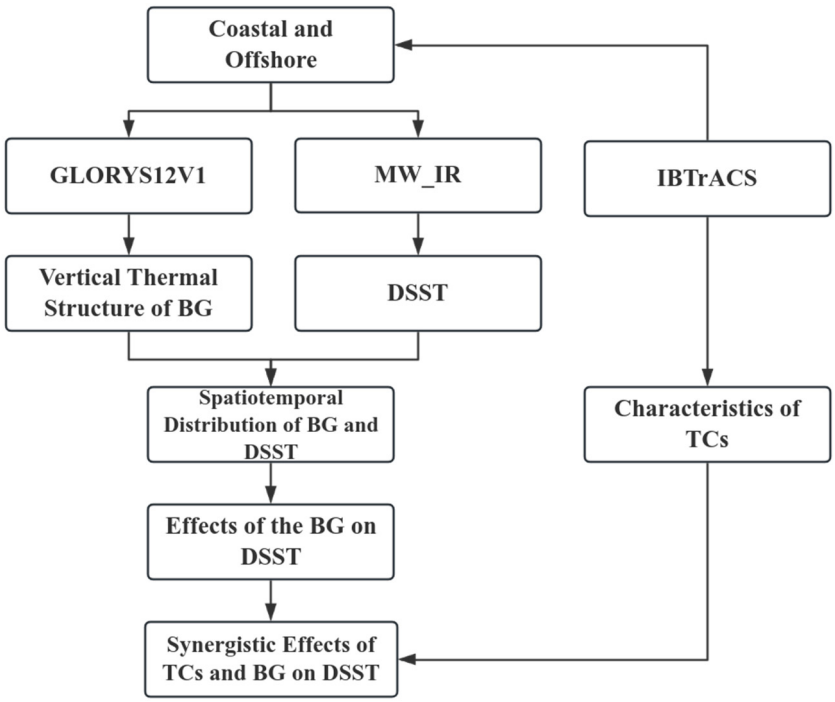


Figure 1. Flowchart of the study.

3. Results

3.1. Spatial and Temporal Distribution of BG and DSST in the WNP

This study compiles the number of TCs and the number of TC observations in the WNP. Figure 2a reveals pronounced TC clustering in the WNP, mainly concentrated to the

west of 140° E between 15° N and 30° N. The highest concentration is near Luzon Island (16° N, 121° E) and decreases outward. During the study period, a total of 376 TCs are recorded. The total number of TC observations in the coastal regions amounted to 6271, while the offshore regions accounted for 7657. The monthly distribution demonstrates strong seasonality, with 73% of coastal region and 74% of offshore region TC occurrences concentrated in July–October, and the highest concentration observed in August. Conversely, January–March accounts for <3% of annual activity, which may have a certain impact on the results of the subsequent analysis (Figure 2b).

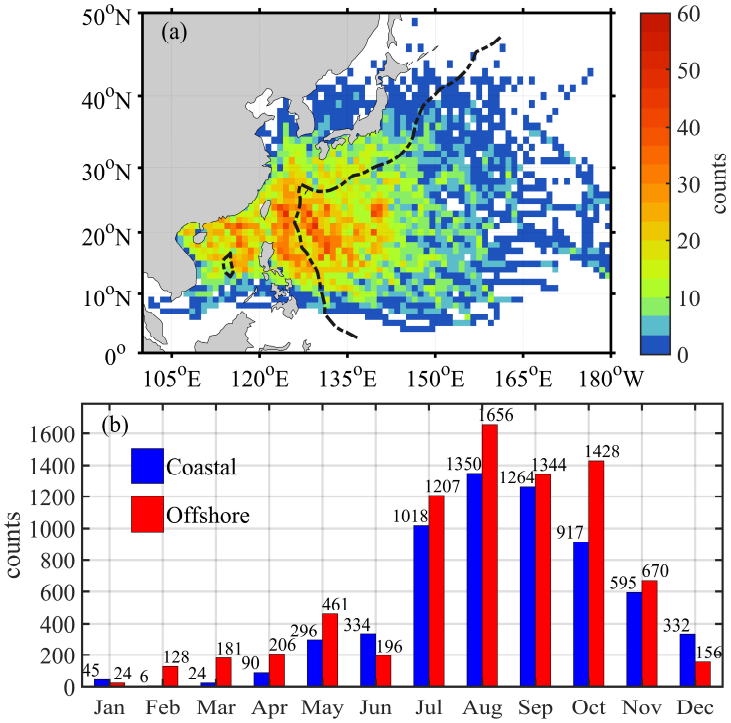


Figure 2. Spatial and temporal distribution of 3-h TC observations in the WNP. (**a**) Spatial distribution of TC observations (2002–2020), calculated on a 1° × 1° grid; (**b**) Monthly distribution of TC observations among coastal (blue) and offshore (red) regions. The black dashed line indicates the 500 km boundary.

The number of TCs exhibits a pronounced seasonal variability. Therefore, this study analyzes the monthly variations of different BG parameters in the WNP. As shown in Figure 3, the climatological monthly variations reveal significant coastal–offshore contrasts in the BG parameters. During the months with a large number of TCs (July–October), the DSST exceeds 0.6 °C, with the maximum exceeding 0.85 °C in September for coastal regions and in August for offshore regions (Figures 2b and 3a). T100 reaches its minimum in August, with the coastal minimum approaching 21 °C and offshore minimum approaching 23 °C, which is even comparable to the coastal maximum in April (Figure 3b). SST-T100 reaches its annual maximum in August, indicating that the vertical temperature gradient between the surface and 100 m depth is conducive to amplifying the DSST induced by TCs (Figure 3c). The MLD and TD generally exhibit a V-shaped distribution, with minimum values occurring in summer, and offshore regions are consistently higher than those in coastal regions across all months. Specifically, the MLD (TD) minimum value is about 25 m (80 m) in coastal regions and about 38 m (90 m) in offshore regions (Figure 3d,g). TS and T Thickness exhibit opposite temporal trends from April to December, with TS demonstrating an increasing trend while T Thickness shows a decreasing trend (Figure 3e,f).

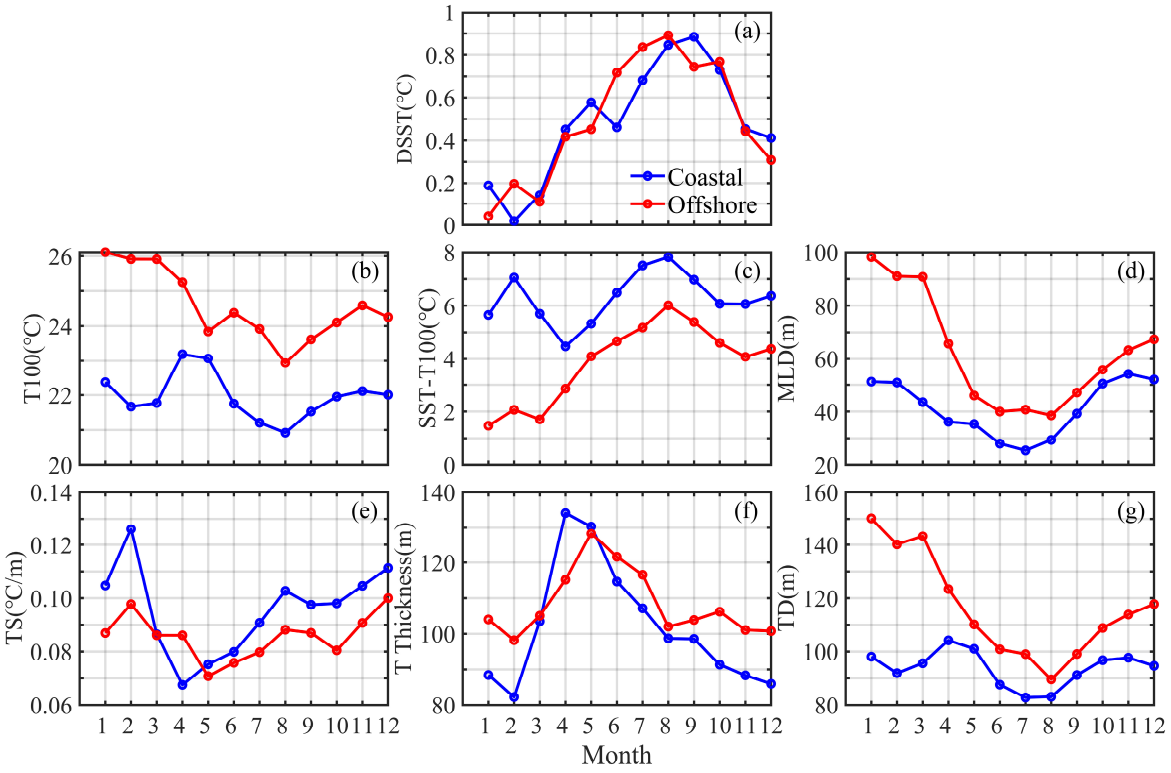


Figure 3. Climatological monthly variations of BG parameters in the WNP. (**a**) DSST; (**b**) T100; (**c**) SST-T100; (**d**) MLD; (**e**) TS; (**f**) T Thickness; (**g**) TD.

Additionally, this study focuses on the climatological spatial distribution of various BG parameters in the WNP. As shown in Figure 4, the spatial pattern of the DSST exhibits a latitudinal gradient, with stronger cooling in the northern regions and lower cooling in the southern regions. This pattern corresponds to the distribution of SST-T100, which generally decreases toward the south, whereas T100 exhibits the opposite trend (Figure 4a–c). In the north of 20° N, shallower MLD and TD enhance cooling, whereas deeper MLD and TD in the south of 20° N are associated with weaker cooling (Figure 4a,d,e). Both T Thickness and TS reach their maximum and minimum values between 10° N and 20° N, and their distribution patterns exhibit some differences compared to DSST (Figure 4a,f,g).

3.2. Effects of the BG on DSST

To further investigate the relationship between DSST and various BG parameters, this study conducts a Spearman correlation analysis between them. Due to the limited amount of data in the first three months, they will be excluded from the overall statistical analysis as well as from the subsequent correlation discussions.

In Table 2, the monthly correlation represents the Spearman correlation between the time series of BG parameters and DSST, both spatially averaged. T100, MLD, T Thickness, and TD exhibit significant negative correlations with DSST, while SST-T100 and TS exhibit positive correlations. Additionally, offshore correlations generally exceed coastal values during the same months. In terms of correlation coefficients, SST-T100 is more significant than T100. Furthermore, T Thickness and TS generally show lower correlations than the other parameters in each month, with more data failing the significance test. Moreover, the correlations of BG parameters tend to be weaker during the summer months. When T Thickness, TD, and TS exhibit a strong correlation with DSST, SST-T100 exhibits a similar correlation, and vice versa. For example, in May for coastal regions (September for offshore regions), the correlation coefficients of T Thickness, TD, and TS with DSST are −0.38 (−0.35), −0.51 (−0.45), and 0.46 (0.22), respectively, while the correlation for SST-T100 is 0.57 (0.47).

Despite the fact that SST-T100, MLD, and TD exhibit the most substantial correlations in the BG parameters, they nevertheless demonstrate relatively weak correlations.

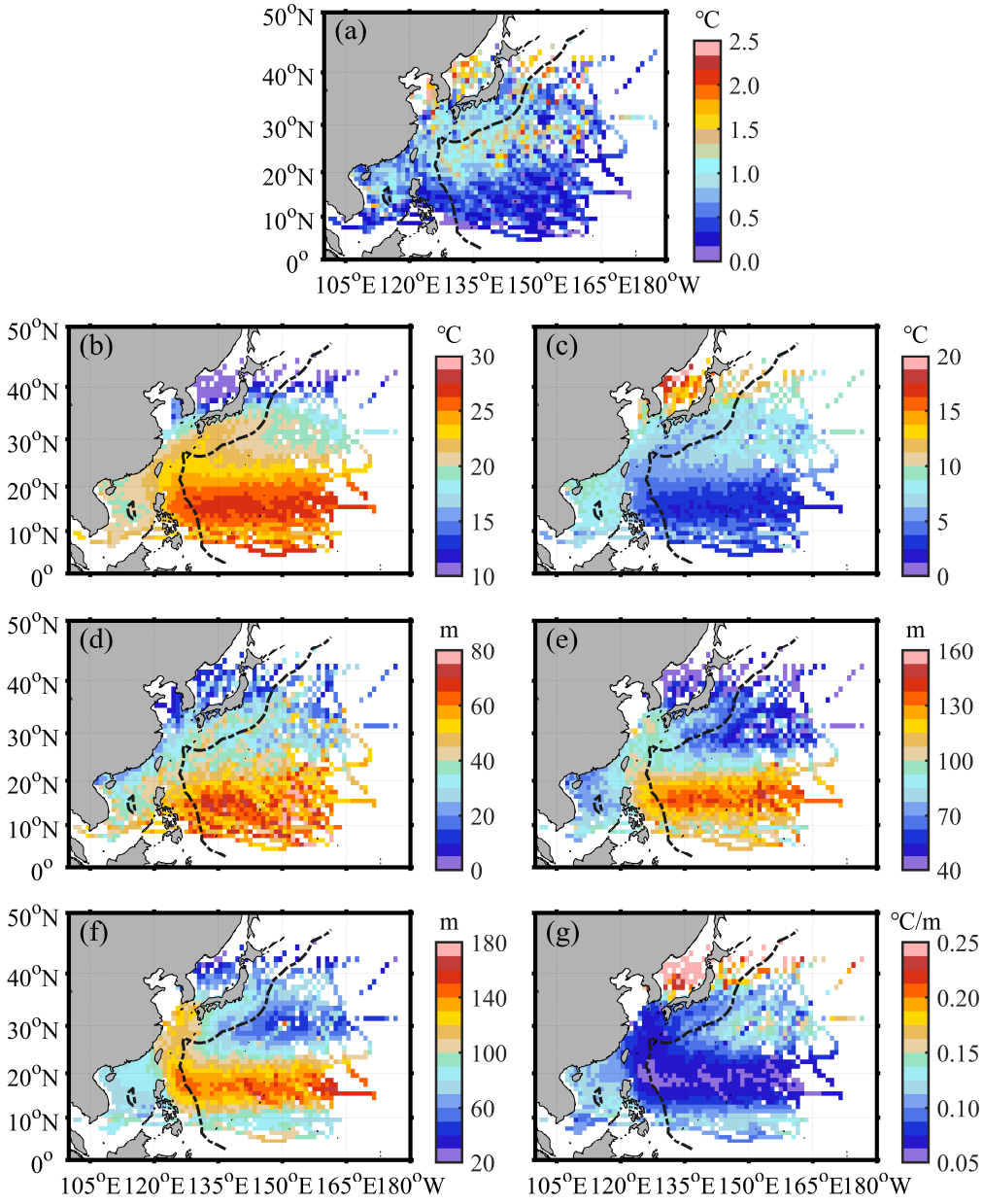


Figure 4. The climatological spatial distribution of the DSST and BG parameters: (**a**) DSST; (**b**) T100; (**c**) SST-T100; (**d**) MLD; (**e**) TD; (**f**) T Thickness; and (**g**) TS. The black dashed line indicates the 500 km boundary.

Building on the above analysis, this study further presents statistical scatter plots of DSST against various BG parameters to examine their correspondence and compare their respective regression fits. Figure 5 illustrates these scatter plots, showing the overall Spearman correlation between the time series of each BG parameter and DSST. The results indicate that T100, MLD, TD, and T Thickness exhibit negative correlations with DSST, whereas SST-T100 and TS demonstrate positive correlations. In addition, the ranges of key BG parameters in coastal and offshore regions show notable differences. For instance, T100, SST-T100, and TS are generally wider in coastal regions than in offshore regions, while MLD, TD, and T Thickness exhibit similar distribution ranges across both regions. However, the MLD and TD in offshore regions are concentrated in deeper depth ranges.

Table 2. Monthly Spearman correlation between BG parameters and DSST (C represents coastal regions, O represents offshore regions, and values marked with an asterisk denote correlations that pass the 95% confidence interval; All excludes data from January to March).

Month	T100		SST−T100		MLD		T Thickness		TD		TS	
	C	O	C	O	C	O	C	O	C	O	C	O
1	−0.31 *	0.63	0.33	−0.83	−0.73	0.83	−0.50	0.70	−0.48	0.84	0.34 *	−0.83
2	−0.94	0.06 *	0.94	0.16 *	−1.00	−0.21	0.94	−0.34	−0.83 *	−0.27	−0.83 *	0.42
3	−0.35 *	−0.18	0.92	0.18	−0.49	−0.35	−0.88	0.42	−0.47	−0.19	0.92	−0.44
4	−0.38	−0.46	0.42	0.40	−0.39	−0.60	−0.21	0.20	−0.47	−0.30	0.31	−0.14
5	−0.13	−0.19	0.57	0.31	−0.31	−0.43	−0.38	−0.06 *	−0.51	−0.39	0.46	−0.05 *
6	0.35	−0.09 *	0.16	0.43	−0.17	−0.39	0.05 *	0.16	−0.08 *	−0.27	0.11	−0.23
7	0.08	−0.32	0.13	0.48	−0.02 *	−0.53	−0.12	−0.22	−0.14	−0.41	0.11	0.15
8	−0.07	−0.16	0.13	0.23	−0.31	−0.24	0.04 *	−0.18	−0.10	−0.22	−0.08	0.15
9	−0.25	−0.39	0.30	0.47	−0.37	−0.50	−0.18	−0.35	−0.32	−0.45	0.16	0.22
10	−0.18	−0.23	0.27	0.24	−0.34	−0.23	−0.19	−0.19	−0.30	−0.23	0.12	0.03 *
11	−0.08	−0.01 *	0.20	−0.14	−0.25	0.15	−0.08	0.05 *	−0.20	0.10	0.16	−0.26
12	−0.45	−0.31	0.40	0.21	−0.44	−0.17	−0.20	−0.11 *	−0.39	−0.22	0.02 *	0.09 *
All	−0.13	−0.27	0.28	0.37	−0.27	−0.40	−0.11	−0.18	−0.25	−0.35	0.08	0.06

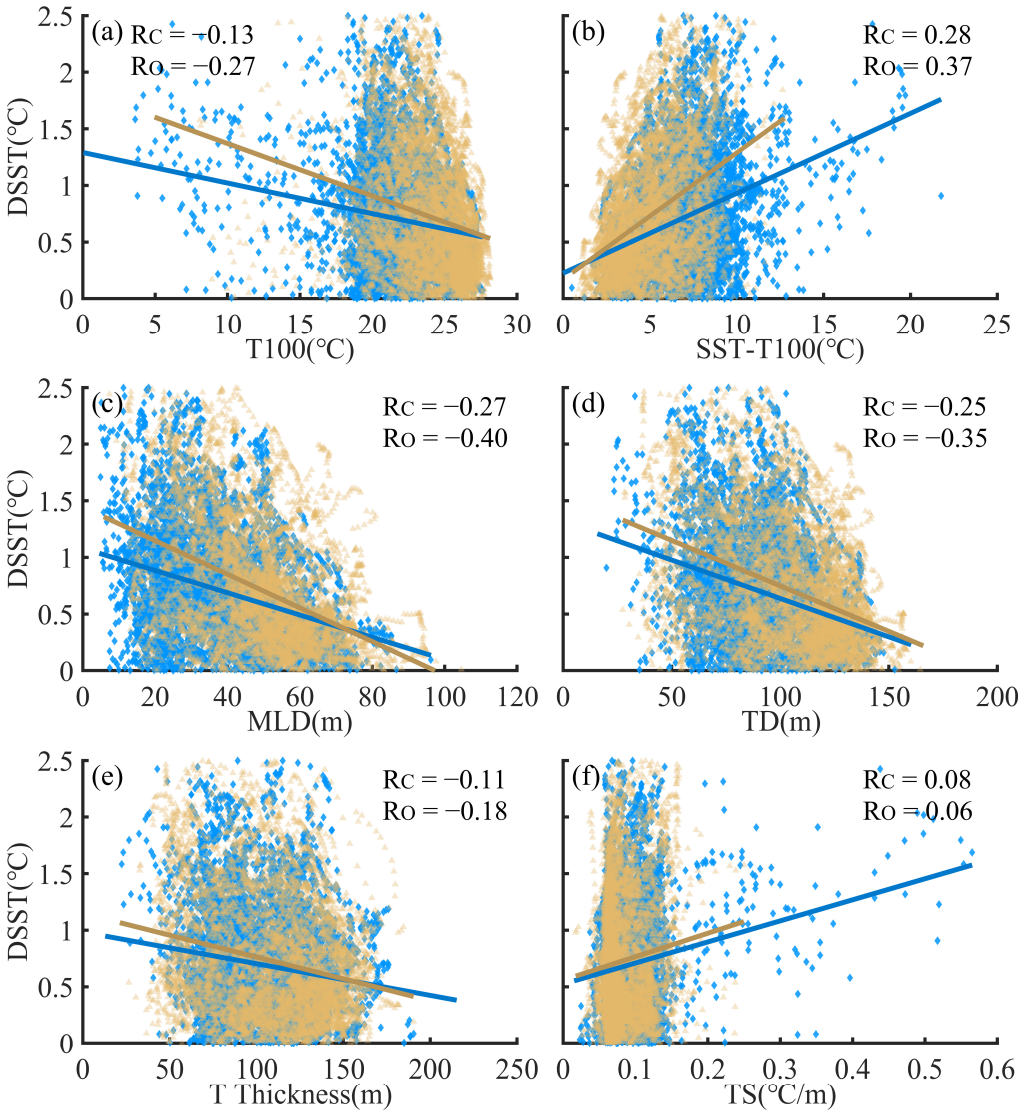


Figure 5. Correlation of the DSST with (**a**) T100; (**b**) SST-T100; (**c**) MLD; (**d**) TD; (**e**) T Thickness; and (**f**) TS. The lines in the figure represent the regression fits (R_C represents coastal regions, blue; R_O represents offshore regions, yellow).

To further investigate the relationship between DSST and various BG parameters, this study presents the spatial distribution of the Spearman temporal correlation between BG parameters and DSST, as shown in Figure 6. The results demonstrate that SST-T100 exhibits a stronger correlation with DSST than T100, with a generally positive correlation across the field. In contrast, MLD and TD show a distinct negative correlation throughout most of the field. Additionally, the Spearman correlations of TS and T Thickness with DSST display an intricate spatial pattern with opposite trends, suggesting that a single variable cannot adequately describe the DSST. To better understand the relationship between BG and DSST, it is necessary to conduct a comprehensive analysis incorporating multiple parameters (Figure 6e,f).

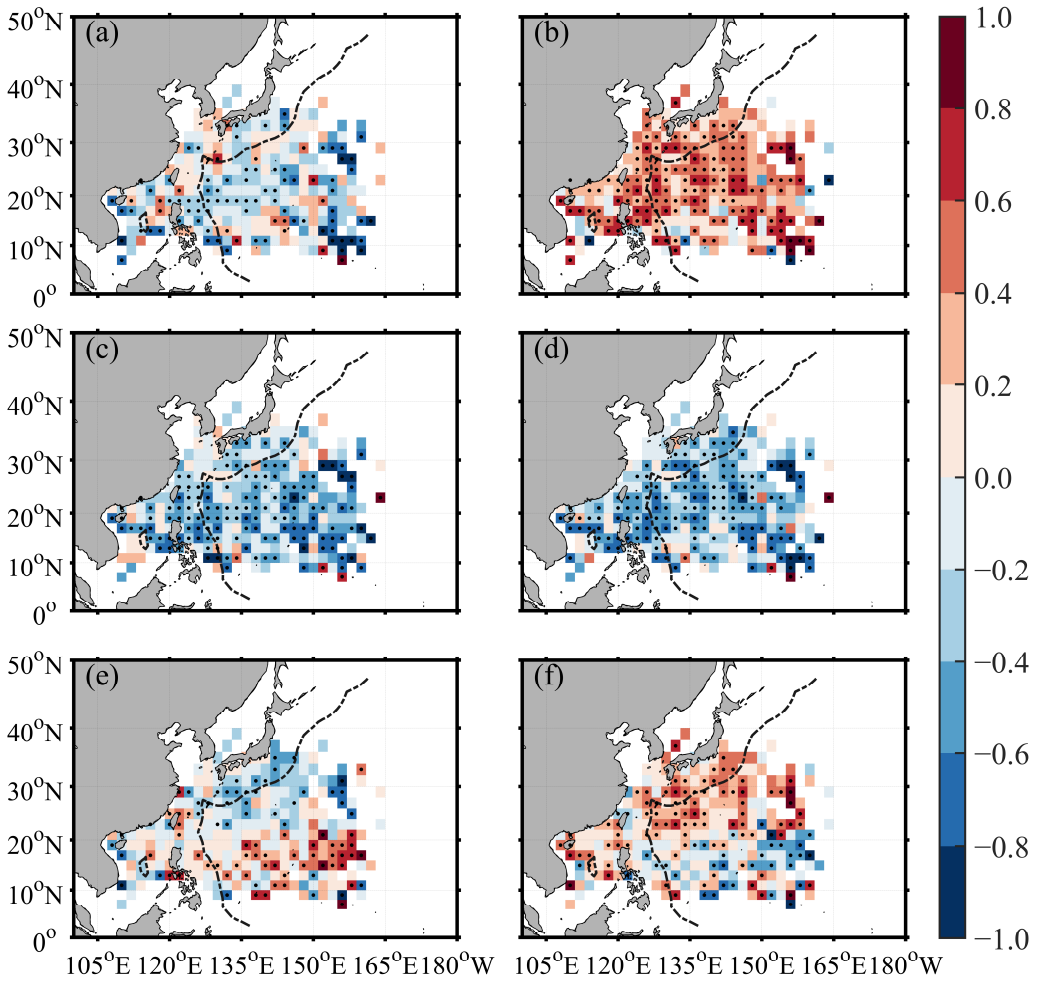


Figure 6. Spatial distribution of the Spearman temporal correlation between BG parameters and DSST. (**a**) T100; (**b**) SST-T100; (**c**) MLD; (**d**) TD; (**e**) T Thickness; (**f**) TS. Black dots represent regions passing the 95% confidence level. The black dashed line indicates the 500 km boundary.

The preceding discussion outlined the relationship between DSST and various BG parameters. To further investigate DSST, this study incorporates TC characteristics (R34, Trans, MW) to assess their influence. Therefore, Figures 7 and 8 illustrate the relationships between TC characteristics (R34, Trans, and MW) and BG parameters (MLD and TD) in relation to DSST. In general, TCs with a large radius, slow movement, and strong maximum sustained winds, along with a shallower MLD and TD, are more likely to induce intense DSST.

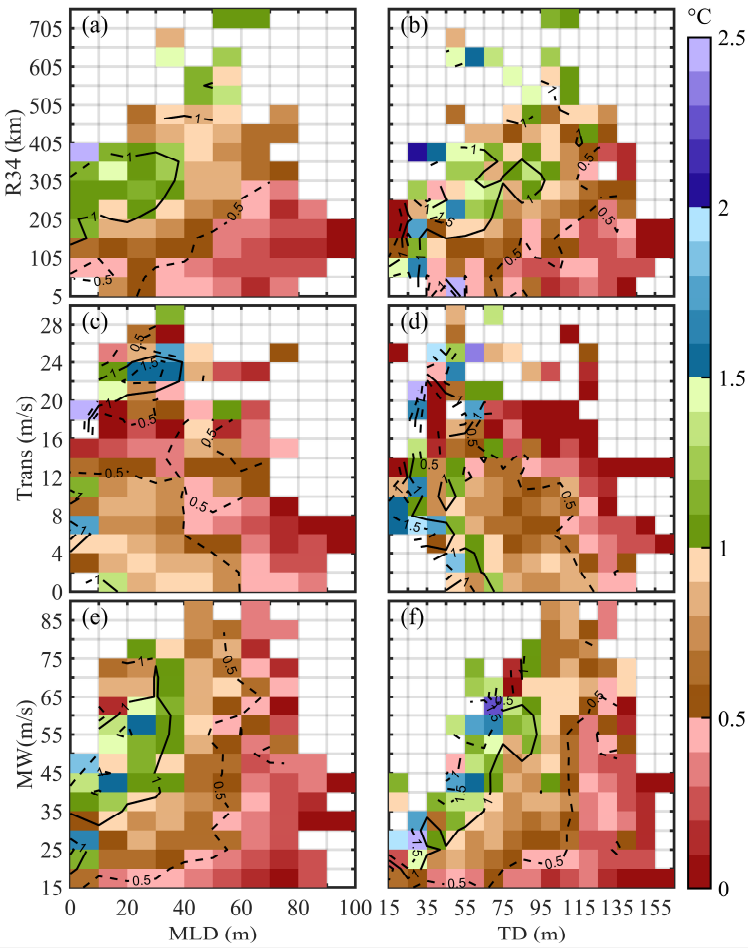


Figure 7. Relationship between coastal DSST and MLD (**left panel**) or TD (**right panel**) under different conditions of (**a**,**b**) R34, (**c**,**d**) Trans and (**e**,**f**) MW. The black solid and dashed lines are contour lines.

In coastal regions, when MLD < 40 m, DSST can exceed 1.5 °C and when TD < 95 m, DSST can easily surpass 1 °C. This suggests that shallow MLD and TD create favorable conditions for stronger DSST. When MLD > 60 m, DSST generally remains below 0.5 °C, regardless of changes in TC characteristics, and when TD > 115 m, DSST rarely exceeds 0.5 °C. This indicates that BG plays a decisive role in limiting DSST. In addition, when R34 > 305 km, DSST can exceed 0.5 °C regardless of MLD variations.

In offshore regions, when MLD > 90 m or TD > 145 m, DSST generally remains below 0.5 °C regardless of TC characteristics, signifying that a deep MLD or TD effectively inhibits DSST. When MLD < 70 m or TD < 115 m, DSST can exceed 1 °C, indicating that shallow MLD and TD create a favorable environment for intense DSST. In addition, when R34 > 320 km, DSST can exceed 0.5 °C, largely independent of MLD or TD variations.

It is clear that both TC characteristics and BG are essential. When the MLD or TD is shallow, even unfavorable TC conditions can induce significant DSST, highlighting the important influence of BG in those conditions. Conversely, large R34 and MW and slow Trans can drive a notable DSST regardless of changes in MLD or TD, reflecting the critical role of TC factors. Hence, no single factor uniformly dominates; rather, the interplay between BG and TC ultimately determines the magnitude of DSST.

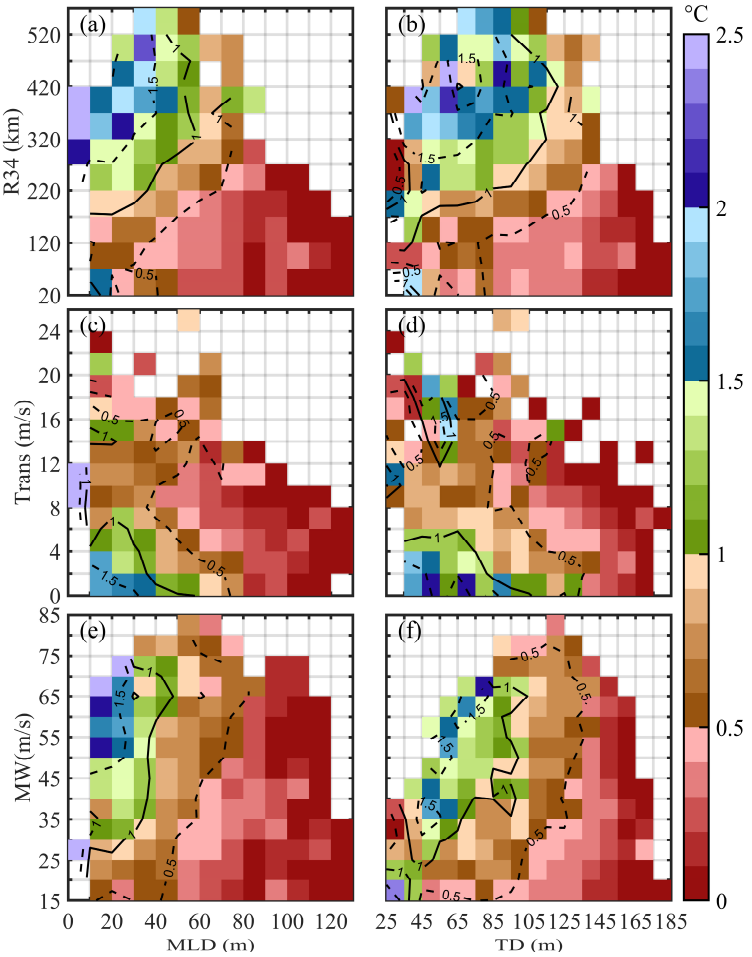


Figure 8. Relationship between offshore DSST and MLD (**left panel**) or TD (**right panel**) under different conditions of (**a**,**b**) R34, (**c**,**d**) Trans, and (**e**,**f**) MW. The black solid and dashed lines are contour lines.

3.3. Synergistic Effects of the BG and TC on DSST

Based on the above analysis, the parameters related to the BG and the characteristics of TC both influence DSST. Larger values of R34 and MW indicate TC characteristics that are favorable for DSST, while larger values of Trans, MLD, and TD reflect TC and BG characteristics that are unfavorable for DSST (Figures 7 and 8). To account for the synergistic effects of TC and BG on DSST, this study introduces the dimensionless parameters R_{mld} and R_{td}.

First, for the TC, a larger MW indicates stronger energy input from the TC into the ocean, while a larger R34 signifies a broader spatial extent of TC-induced energy input. Additionally, a slower Trans implies a prolonged duration of TC influence which allows the TC's wind energy input to the same area for a longer time, leading to more pronounced DSST. To comprehensively account for the influence of TC, the TC index (TCI) was formulated,

$$TCI = \frac{MW \times R_{34}}{Trans} \quad (5)$$

Next, MLD and TD characterize the influence of the BG on DSST, as they regulate vertical mixing efficiency. Deeper MLD and TD reduce the intensity of DSST, highlighting the constraining effect of the BG on DSST. In contrast, the TCI represents the TC's capacity to

enhance DSST [31]. To capture the synergistic effects of TC and BG on DSST, dimensionless indices R_{mld} and R_{td} are formulated as follows:

$$R_{mld} = \frac{TCI}{MLD} \quad (6)$$

$$R_{td} = \frac{TCI}{TD} \quad (7)$$

The indices R_{mld} and R_{td} represent the synergistic effects of the TC and the BG on DSST. These dimensionless metrics quantify the synergistic effects of TC-driven forcing (enhancing cooling through energy input) and oceanic suppression (inhibiting cooling via stratification) in promoting a DSST.

To analyze R_{mld} and R_{td}, this study presents their climatological spatial distribution and monthly variations, as illustrated in Figure 9 for both coastal and offshore regions. R_{mld} and R_{td} exhibit similar spatial and temporal distribution. The climatological spatial distribution reveals that in coastal regions, R_{mld} and R_{td} reach their maximum values at 20° N–30° N, gradually decreasing toward both sides of the latitude.

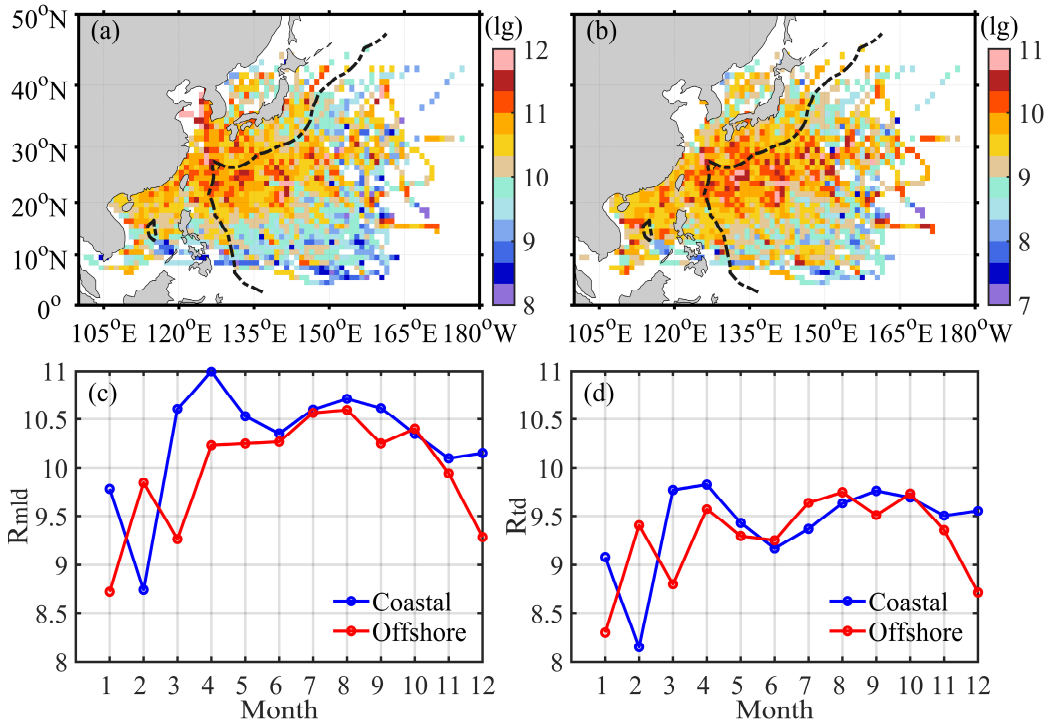


Figure 9. Climatological spatial and temporal distribution of (**a**,**c**) R_{mld} and (**b**,**d**) R_{td}. Values are shown as lg. The black dashed line indicates the 500 km boundary.

From the climatological monthly temporal distribution of R_{mld} and R_{td}, it can be observed that in coastal regions, R_{mld} and R_{td} reach their maximum values in April, whereas in offshore regions, their peaks occur in August. The peak values of R_{mld} exceed 10.5 in both regions, while R_{td} peaks are above 9.5, with R_{mld} generally larger than R_{td} during the same period. R_{mld} and R_{td} exhibit a similar spatial and temporal distribution to DSST in both coastal and offshore regions. This indicates that the magnitudes of R_{mld} and R_{td} can be used to characterize the intensity of DSST. Therefore, R_{mld} and R_{td} values exhibit a positive correlation with DSST (Figures 3a, 4a and 9).

To explore and evaluate the representational capability of the R_{mld} and R_{td} for DSST, this study conducts a correlation analysis between R_{mld} and R_{td} with DSST. Table 3 shows the results of the monthly Spearman correlation analysis. From April to December, R_{mld}

and R_{td} both show a stable positive correlation with DSST, generally showing a more significant correlation in offshore regions compared to coastal regions. In coastal regions, the correlation coefficients of R_{mld} and R_{td} peak in May at 0.77 and 0.80, respectively, while in offshore regions, they peak in April at 0.84 and 0.77. Additionally, almost all data pass significance tests. Quantitative comparison in Table 2 reveals that R_{mld} and R_{td} exhibit stronger correlations with DSST than MLD and TD, indicating that the incorporation of the TC characteristics alongside the BG parameters provides a more comprehensive description of the DSST.

Table 3. Monthly Spearman correlation analysis between R_{mld} and R_{td} with DSST (C represents coastal regions, O represents offshore regions, values marked with an asterisk denote correlations that pass the 95% confidence interval; All excludes data from January to March).

Month	R_{mld}		R_{td}	
	C	O	C	O
1	0.58	−0.50	0.55	−0.50
2	−0.09 *	−0.07 *	−0.60 *	−0.06 *
3	0.67	0.43	0.70	0.40
4	0.43	0.84	0.53	0.77
5	0.77	0.59	0.80	0.52
6	0.46	0.48	0.49	0.36
7	0.54	0.65	0.61	0.60
8	0.60	0.73	0.52	0.70
9	0.37	0.63	0.34	0.62
10	0.53	0.68	0.53	0.68
11	0.43	0.59	0.41	0.60
12	0.44	0.56	0.41	0.57
All	0.53	0.66	0.50	0.63

Although more intense TCs generally lead to larger DSST, the increased correlations between R_{mld} and DSST, as well as R_{td} and DSST, indicate that these indices offer a more effective representation of the complex interplay between TC and BG. Specifically, they help capture cases where relatively weak TCs—when occurring under favorable oceanic backgrounds—can induce greater surface cooling than stronger TCs under less favorable conditions. By integrating both TC and BG into unified indices, R_{mld} and R_{td} provide a more comprehensive and physically grounded framework for analyzing DSST responses.

Building on the above analysis, Figure 10 presents scatter plots of DSST against R_{mld} and R_{td}, showing their overall Spearman correlation and demonstrating that both metrics generally exhibit a more pronounced positive correlation with DSST. The values of the R_{mld} are concentrated between seven and thirteen, while R_{td} values range from six to twelve, with a similar distribution in both coastal and offshore regions. The correlation coefficients of the MLD and TD with DSST are −0.27 (−0.40) and −0.25 (−0.35) for coastal (offshore) regions, respectively. When further considering the TC characteristics, the correlation coefficients of R_{mld} and R_{td} with DSST increase to 0.53 (0.66) and 0.50 (0.63).

To further investigate the relationship between DSST and these two dimensionless metrics, this study also presents the spatial distribution of their Spearman temporal correlation coefficients with DSST, as shown in Figure 11. Both R_{mld} and R_{td} exhibit more consistent and significant correlations with DSST than MLD and TD, and show a broader spatial extent that passes the significance test (Figures 6 and 11).

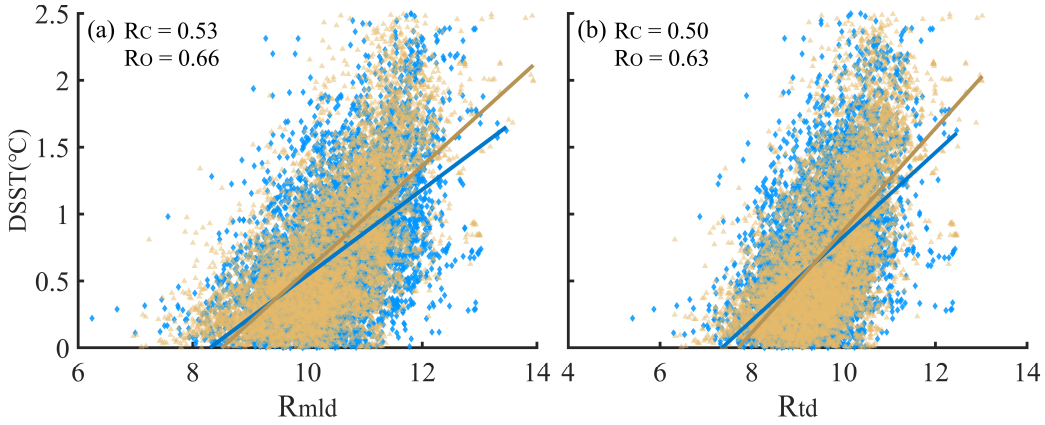


Figure 10. Same as Figure 5 but for (**a**) R_{mld} and (**b**) R_{td} (R_C represents coastal regions, blue; R_O represents offshore regions, yellow).

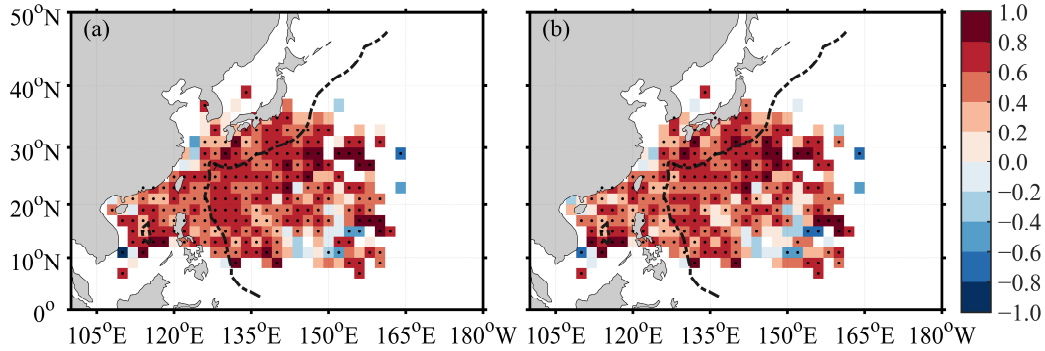


Figure 11. Same as Figure 6. But for (**a**) R_{mld} and (**b**) R_{td}. The black dashed line indicates the 500 km boundary.

R_{mld} and R_{td} comprehensively consider the maximum sustained wind speed, the translation speed, the 34-kt wind radius of the TC, and the BG conditions. Consequently, in describing DSST, R_{mld} and R_{td} provide more stable and robust representation compared to solely using BG parameters.

4. Discussion

DSST is defined as the SST difference between 1–5 days before and after the passage of each TC. This time window is supported by previous studies showing that SST typically recovers to its climatological state within 5 days, and that the most significant cooling occurs during this period [8]. A spatial domain of 6° × 6° centered on the TC location is used, which encompasses the typical wind radius (~300 km) where SST responses are most pronounced. Jin et al. [66] have shown that while the magnitude of DSST may vary with different temporal and spatial scales, the overall seasonal and spatial patterns remain consistent, supporting the robustness of this approach.

Da et al. [24] analyzed TC parameters (Vmax, Vtrans, and R34) and BG parameters (Grad-T, Grad-S, and MLD) across individual ocean basins. The spatial distributions of the MLD and DSST, as well as their correlations in the WNP, are similar to those presented in this study (Figures 4 and 6). Beyond MLD, our findings demonstrate that the correlation between SST-T100 and DSST was also higher than that of T100 (Table 2), which is consistent with Vincent et al. [56], who pointed out that SST-T100 actually improved the ability to predict TC. In addition, this study primarily investigates the correlations between BG parameters (T100, SST-T100, MLD, TD, T Thickness, and TS) and DSST (Figure 5). In contrast, Pun et al. [35] focused on the correlations of R34, Vmax, translation speed (Uh), and upper ocean heat content (UOHC) with DSST, presenting values of 0.49, 0.46,

−0.38, and −0.37, respectively. Consequently, whether considering BG or TC parameters individually, their correlations with DSST rarely exceed 0.5. However, when BG and TC parameters are combined, as demonstrated in this study, the correlation increases (Figure 11). Furthermore, compared to MLD and TD, the R_{mld} and R_{td} exhibit more stable correlations with DSST across both spatial and temporal scales (Figure 12).

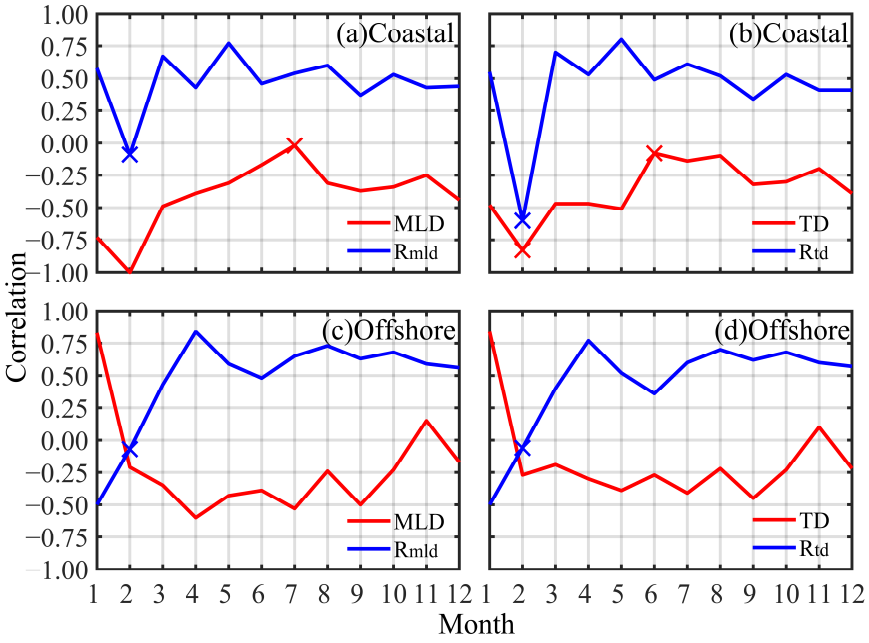


Figure 12. Comparative analysis of the correlation between the BG parameters (red line) and the metrics (R_{mld} and R_{td}, blue line) with DSST. (The symbol × denotes a failure to achieve the 95% significance level). The upper panel shows coastal regions and the lower panel shows offshore regions.

Our results show that coastal regions correlation between R_{mld} and R_{td} with DSST exceed 0.75 in May, maintaining values around 0.5 in other months with small seasonal variation (Table 3, Figure 12). In offshore regions, the maximum correlation reaches above 0.75 in April, remaining near 0.5 during most other months. In contrast, Spearman correlations involving MLD and TD exhibit substantial monthly variability in both coastal and offshore regions, even switching between positive and negative values. These findings indicate that R_{mld} and R_{td} to some extent enhance correlations with DSST.

In this study, we construct dimensionless parameters R_{mld} and R_{td} to characterize DSST. In addition, there are also many other excellent approaches to describe it. Oey [57] proposed a dimensionless (nonlinear) function Ψ representing DSST, determined by both TC parameters and upper-layer BG characteristics, and the explained variance in their results is $r^2 \approx 0.6$. Cui et al. [36] built a model using an efficient and robust machine learning-based method with 12 predictors related to TC characteristics and pre-storm ocean states. Their findings indicate that TC intensity, translation speed, size, pre-storm MLD, and SST are the dominant factors in determining the magnitude of the SST response. Moreover, Vincent et al. [12] introduced the Wind Power Index (WPi) and Cooling Inhibition Index (CI). WPi primarily considered DSST impacts from TC parameters such as MW, translation speed, and size, while CI explained the pre-TC upper-ocean stratification resistance to DSST. Therefore, WPi and CI describe DSST variability from TC and BG perspectives. The R_{mld} and R_{td} proposed in this study systematically incorporates the synergistic effects of BG and TC, achieving a more comprehensive analysis of DSST.

5. Conclusions

Based on the satellite observation data and reanalysis data, this study analyzes the distribution characteristics of the DSST under TC conditions in the WNP as well as the impacts of the TC characteristics and BG structure on the DSST. Further, combining the TC and BG parameters, this study proposes the dimensionless metrics R_{mld} and R_{td} to better characterize the spatial and temporal distribution of the DSST.

In the WNP, the magnitude of DSST exhibits significant temporal and spatial variation. The majority of the TC occurrences are concentrated from July to October in both coastal and offshore regions, with the DSST amplitude exceeding 0.6 °C. DSST reaches its maximum in September for coastal regions and in August for offshore regions, with both exceeding 0.85 °C (Figures 2b and 3a).

In terms of the BG parameters, MLD and TD are effective in representing DSST. The correlations of MLD and TD with DSST in offshore regions are −0.40 and −0.35, respectively, which is more significant than the correlations of −0.27 and −0.25 in coastal regions (Figure 5c,d). However, it is insufficient to only consider BG factors; therefore, we also take the impact of TCs into account. In coastal regions, when MLD > 60 m, DSST generally remains below 0.5 °C, regardless of changes in TC characteristics, and when TD > 115 m, DSST rarely exceeds 1 °C. In addition, when R34 > 305 km, DSST can exceed 0.5 °C regardless of MLD variations. In offshore regions, when MLD > 90 m or TD > 145 m, DSST generally remains below 0.5 °C regardless of TC characteristics. In addition, when R34 > 320 km, DSST can exceed 0.5 °C, largely independent of MLD or TD variations. It is clear that the interplay between BG and TC ultimately determines the magnitude of DSST. Based on the above analysis, larger values of R34 and MW are favorable for DSST, while larger values of Trans, MLD, and TD are unfavorable for DSST (Figures 7 and 8). To account for the synergistic effects of TC and BG on DSST, this study introduces the dimensionless parameters R_{mld} and R_{td}.

In both temporal and spatial dimensions, R_{mld} and R_{td} can better characterize DSST than MLD and TD. The Spearman correlations of R_{mld} and R_{td} with coastal DSST can reach 0.53 and 0.50, respectively, while in offshore regions, the correlations are up to 0.66 and 0.63. Moreover, the correlations exhibit greater spatial consistency and better pass the test of significance (Figures 5, 6 and 10–12). Since R_{mld} and R_{td} incorporate TC parameters such as MW, Trans, R34, and the BG conditions, the R_{mld} and R_{td} are more stable across different seasons, making them more representative than the solely BG parameters. Indeed, more intense TCs tend to produce a larger DSST, which is consistent with existing literature. However, the novel contribution of this study lies in its comprehensive approach. The key innovation here is not just the expected correlation between TC or BG and DSST, but the ability to capture cases where relatively weak TCs—when occurring under favorable oceanic backgrounds—can induce greater surface cooling than stronger TCs under less favorable conditions. This insight improves our understanding of the complex interaction between TCs and BG, enabling better forecasting of DSST and related phenomena in different TC scenarios.

This study specifically focuses on the oceanic conditions prior to the arrival of TCs. Incorporating parameters such as R_{mld} and R_{td} captures the synergistic effects of BG and TC on DSST. This approach enables us to estimate and provide early warnings for areas that will soon be affected by the TCs. Specifically, by predicting the changes in DSST before the TC reaches the coast, we improve our ability to forecast TC intensity and anticipate potential impacts, which is critical for disaster preparedness and mitigation in coastal regions. But in constructing the indices, only the more significant temporal and spatial correlations of MLD and TD are considered, and the more complex TS and T Thickness are not considered. Future studies should systematically explore the synergistic effects of

various BG and TC parameters on the DSST. Moreover, while investigating the ocean's response to TCs, it is also crucial to analyze the ocean's impact on the TCs.

Author Contributions: Conceptualization, C.Y. and R.R.; methodology, R.R.; software, C.Y. and R.R.; validation, C.Y. and R.R.; formal analysis, R.R. and C.Y.; investigation, R.R. and P.B.; resources, C.Y.; data curation, R.R., P.B. and B.L.; writing—original draft preparation, C.Y. and R.R.; writing—review and editing, C.Y.; visualization, R.R.; supervision, C.Y.; project administration, C.Y.; funding acquisition, C.Y., P.B. and B.L. All authors have read and agreed to the published version of the manuscript.

Funding: This study was supported by the National Natural Science Foundation of China (42406019), the National Natural Science Foundation of China (42449903), the Special Fund for Zhejiang Ocean University from Bureau of Science and Technology of Zhoushan (2023C41006), and the National Natural Science Foundation of China (42106017).

Data Availability Statement: The global tropical cyclone location and intensity data from IBTrACS can be accessed at https://www.ncei.noaa.gov/products/international-best-track-archive (accessed on 15 March 2024). The satellite sea surface temperature dataset (MW_IR) from Remote Sensing Systems can be accessed at https://data.remss.com/SST/daily/mw_ir/v05.1/netcdf (accessed on 20 March 2024). Subsurface temperature from the GLORYS12V1 reanalysis product can be accessed at https://data.marine.copernicus.eu/product/GLOBAL_MULTIYEAR_PHY_001_030 (accessed on 16 May 2024).

Conflicts of Interest: The authors declare no conflicts of interest.

References

1. Emanuel, K. Tropical Cyclones. *Annu. Rev. Earth Planet. Sci.* **2003**, *31*, 75–104. [CrossRef]
2. Li, A.; Guan, S.; Mo, D.; Hou, Y.; Hong, X.; Liu, Z. Modeling Wave Effects on Storm Surge from Different Typhoon Intensities and Sizes in the South China Sea. *Estuar. Coast. Shelf Sci.* **2020**, *235*, 106551. [CrossRef]
3. Emanuel, K.A. Thermodynamic Control of Hurricane Intensity. *Nature* **1999**, *401*, 665–669. [CrossRef]
4. Jin, F.-F.; Boucharel, J.; Lin, I.-I. Eastern Pacific Tropical Cyclones Intensified by El Niño Delivery of Subsurface Ocean Heat. *Nature* **2014**, *516*, 82–85. [CrossRef]
5. Lin, I.-I.; Black, P.; Price, J.F.; Yang, C.-Y.; Chen, S.S.; Lien, C.-C.; Harr, P.; Chi, N.-H.; Wu, C.-C.; D'Asaro, E.A. An Ocean Coupling Potential Intensity Index for Tropical Cyclones. *Geophys. Res. Lett.* **2013**, *40*, 1878–1882. [CrossRef]
6. Mei, W.; Xie, S.-P.; Primeau, F.; McWilliams, J.C.; Pasquero, C. Northwestern Pacific Typhoon Intensity Controlled by Changes in Ocean Temperatures. *Sci. Adv.* **2015**, *1*, e1500014. [CrossRef] [PubMed]
7. Bracken, W.E.; Bosart, L.F. The Role of Synoptic-Scale Flow during Tropical Cyclogenesis over the North Atlantic Ocean. *Mon. Weather. Rev.* **2000**, *128*, 353–376. [CrossRef]
8. Dare, R.A.; McBride, J.L. Sea Surface Temperature Response to Tropical Cyclones. *Mon. Weather Rev.* **2011**, *139*, 3798–3808. [CrossRef]
9. Gray, W. Global View of the Origin of Tropical Disturbances and Storms. *Mon. Weather Rev.* **1968**, *96*, 669–700. [CrossRef]
10. Cione, J.J.; Uhlhorn, E.W. Sea Surface Temperature Variability in Hurricanes: Implications with Respect to Intensity Change. *Mon. Weather Rev.* **2003**, *131*, 1783–1796. [CrossRef]
11. Price, J.F. Upper Ocean Response to a Hurricane. *J. Phys. Oceanogr.* **1981**, *11*, 153–175. [CrossRef]
12. Vincent, E.M.; Lengaigne, M.; Madec, G.; Vialard, J.; Samson, G.; Jourdain, N.C.; Menkes, C.E.; Jullien, S. Processes Setting the Characteristics of Sea Surface Cooling Induced by Tropical Cyclones. *J. Geophys. Res. Oceans* **2012**, *117*, C02020. [CrossRef]
13. Lin, I.-I.; Pun, I.-F.; Wu, C.-C. Upper-Ocean Thermal Structure and the Western North Pacific Category 5 Typhoons. Part II: Dependence on Translation Speed. *Mon. Weather Rev.* **2009**, *137*, 3744–3757. [CrossRef]
14. Shay, L.K.; Brewster, J.K. Oceanic Heat Content Variability in the Eastern Pacific Ocean for Hurricane Intensity Forecasting. *Mon. Weather Rev.* **2010**, *138*, 2110–2131. [CrossRef]
15. Glenn, S.M.; Miles, T.N.; Seroka, G.N.; Xu, Y.; Forney, R.K.; Yu, F.; Roarty, H.; Schofield, O.; Kohut, J. Stratified Coastal Ocean Interactions with Tropical Cyclones. *Nat. Commun.* **2016**, *7*, 10887. [CrossRef]
16. Guan, S.; Zhao, W.; Sun, L.; Zhou, C.; Liu, Z.; Hong, X.; Zhang, Y.; Tian, J.; Hou, Y. Tropical Cyclone-Induced Sea Surface Cooling over the Yellow Sea and Bohai Sea in the 2019 Pacific Typhoon Season. *J. Mar. Syst.* **2021**, *217*, 103509. [CrossRef]
17. Mahapatra, D.K.; Rao, A.D.; Babu, S.V.; Srinivas, C. Influence of Coast Line on Upper Ocean's Response to the Tropical Cyclone. *Geophys. Res. Lett.* **2007**, *34*, L17603. [CrossRef]

18. Shen, W.; Ginis, I. Effects of Surface Heat Flux-Induced Sea Surface Temperature Changes on Tropical Cyclone Intensity. *Geophys. Res. Lett.* **2003**, *30*, 1933. [CrossRef]
19. Greatbatch, R.J. On the Response of the Ocean to a Moving Storm: Parameters and Scales. *J. Phys. Oceanogr.* **1984**, *14*, 59–78. [CrossRef]
20. Jacob, S.D.; Shay, L.K.; Mariano, A.J.; Black, P.G. The 3D Oceanic Mixed Layer Response to Hurricane Gilbert. *J. Phys. Oceanogr.* **2000**, *30*, 1407–1429. [CrossRef]
21. Lin, S.; Zhang, W.-Z.; Shang, S.-P.; Hong, H.-S. Ocean Response to Typhoons in the Western North Pacific: Composite Results from Argo Data. Deep Sea Res. *Part Oceanogr. Res. Pap.* **2017**, *123*, 62–74. [CrossRef]
22. Peng, Y.; Tian, D.; Zhou, F.; Zhang, H.; Ma, X.; Zeng, D.; Meng, Q.; Zhou, B.; Ye, R.; Chen, Y.; et al. Observed Oceanic Response to Tropical Cyclone Amphan (2020) from a Subsurface Mooring in the Bay of Bengal. *Prog. Oceanogr.* **2023**, *219*, 103148. [CrossRef]
23. Shay, L.K.; Black, P.G.; Mariano, A.J.; Hawkins, J.D.; Elsberry, R.L. Upper Ocean Response to Hurricane Gilbert. *J. Geophys. Res. Oceans* **1992**, *97*, 20227–20248. [CrossRef]
24. Da, N.D.; Foltz, G.R.; Balaguru, K.; Fernald, E. Stronger Tropical Cyclone–Induced Ocean Cooling in Near-Coastal Regions Compared to the Open Ocean. *J. Clim.* **2023**, *36*, 6447–6463. [CrossRef]
25. Zheng, Y.; Ma, Z.; Tang, J.; Zhang, Z. The Coastal Effect on Ahead-of-Eye-Center Cooling Induced by Tropical Cyclones. *J. Phys. Oceanogr.* **2023**, *53*, 1519–1534. [CrossRef]
26. Chiang, T.-L.; Wu, C.-R.; Oey, L.-Y. Typhoon Kai-Tak: An Ocean's Perfect Storm. *J. Phys. Oceanogr.* **2011**, *41*, 221–233. [CrossRef]
27. Guan, S.; Zhao, W.; Huthnance, J.; Tian, J.; Wang, J. Observed Upper Ocean Response to Typhoon Megi (2010) in the Northern South China Sea. *J. Geophys. Res. Oceans* **2014**, *119*, 3134–3157. [CrossRef]
28. Ren, D.; Han, S.; Wang, S. Upper Ocean Responses to Tropical Cyclone Mekunu (2018) in the Arabian Sea. *J. Mar. Sci. Eng.* **2024**, *12*, 1177. [CrossRef]
29. Bender, M.A.; Ginis, I.; Kurihara, Y. Numerical Simulations of Tropical Cyclone-Ocean Interaction with a High-Resolution Coupled Model. *J. Geophys. Res. Atmos.* **1993**, *98*, 23245–23263. [CrossRef]
30. Lin, I.-I.; Wu, C.-C.; Emanuel, K.A.; Lee, I.-H.; Wu, C.-R.; Pun, I.-F. The Interaction of Supertyphoon Maemi (2003) with a Warm Ocean Eddy. *Mon. Weather Rev.* **2005**, *133*, 2635. [CrossRef]
31. Price, J.F. Internal Wave Wake of a Moving Storm. Part I. Scales, Energy Budget and Observations. *J. Phys. Oceanogr.* **1983**, *13*, 949–965. [CrossRef]
32. Pun, I.-F.; Lin, I.-I.; Lien, C.-C.; Wu, C.-C. Influence of the Size of Supertyphoon Megi (2010) on SST Cooling. *Mon. Weather Rev.* **2018**, *146*, 661–677. [CrossRef]
33. Pun, I.-F.; Chan, J.C.L.; Lin, I.-I.; Chan, K.T.F.; Price, J.F.; Ko, D.S.; Lien, C.-C.; Wu, Y.-L.; Huang, H.-C. Rapid Intensification of Typhoon Hato (2017) over Shallow Water. *Sustainability* **2019**, *11*, 3709. [CrossRef]
34. Wang, H.; Li, J.; Song, J.; Leng, H.; Wang, H.; Zhang, Z.; Zhang, H.; Zheng, M.; Yang, X.; Wang, C. The Abnormal Track of Super Typhoon Hinnamnor (2022) and Its Interaction with the Upper Ocean. *Deep. Sea Res. Part Oceanogr. Res. Pap.* **2023**, *201*, 104160. [CrossRef]
35. Pun, I.-F.; Knaff, J.A.; Sampson, C.R. Uncertainty of Tropical Cyclone Wind Radii on Sea Surface Temperature Cooling. *J. Geophys. Res. Atmos.* **2021**, *126*, e2021JD034857. [CrossRef]
36. Cui, H.; Tang, D.; Mei, W.; Liu, H.; Sui, Y.; Gu, X. Predicting Tropical Cyclone-Induced Sea Surface Temperature Responses Using Machine Learning. *Geophys. Res. Lett.* **2023**, *50*, e2023GL104171. [CrossRef]
37. Moon, I.-J.; Kwon, S.J. Impact of Upper-Ocean Thermal Structure on the Intensity of Korean Peninsular Landfall Typhoons. *Prog. Oceanogr.* **2012**, *105*, 61–66. [CrossRef]
38. Balaguru, K.; Foltz, G.R.; Leung, L.R.; Hagos, S.M. Impact of Rainfall on Tropical Cyclone-Induced Sea Surface Cooling. *Geophys. Res. Lett.* **2022**, *49*, e2022GL098187. [CrossRef]
39. D'Asaro, E.A.; Black, P.G.; Centurioni, L.R.; Chang, Y.-T.; Chen, S.S.; Foster, R.C.; Graber, H.C.; Harr, P.; Hormann, V.; Lien, R.-C.; et al. Impact of Typhoons on the Ocean in the Pacific. *Bull. Am. Meteorol. Soc.* **2014**, *95*, 1405–1418. [CrossRef]
40. Knaff, J.A.; DeMaria, M.; Sampson, C.R.; Peak, J.E.; Cummings, J.; Schubert, W.H. Upper Oceanic Energy Response to Tropical Cyclone Passage. *J. Clim.* **2013**, *26*, 2631–2650. [CrossRef]
41. Lin, I.-I.; Rogers, R.F.; Huang, H.-C.; Liao, Y.-C.; Herndon, D.; Yu, J.-Y.; Chang, Y.-T.; Zhang, J.A.; Patricola, C.M.; Pun, I.-F.; et al. A Tale of Two Rapidly Intensifying Supertyphoons: Hagibis (2019) and Haiyan (2013). *Bull. Am. Meteorol. Soc.* **2021**, *102*, E1645–E1664. [CrossRef]
42. Mei, W.; Lien, C.-C.; Lin, I.-I.; Xie, S.-P. Tropical Cyclone–Induced Ocean Response: A Comparative Study of the South China Sea and Tropical Northwest Pacific. *J. Clim.* **2015**, *28*, 5952–5968. [CrossRef]
43. Potter, H.; DiMarco, S.F.; Knap, A.H. Tropical Cyclone Heat Potential and the Rapid Intensification of Hurricane Harvey in the Texas Bight. *J. Geophys. Res. Oceans* **2019**, *124*, 2440–2451. [CrossRef]

44. Zhuang, Z.; Yang, Y.; Shu, Q.; Song, Z.; Zhao, B.; Yuan, Y. Variability of Non-Breaking Surface-Wave Induced Mixing and Its Effects on Ocean Thermodynamical Structure in the Northwest Pacific during Typhoon Lekima (2019). *Deep. Sea Res. Part Oceanogr. Res. Pap.* **2023**, *202*, 104178. [CrossRef]
45. Chan, J.C.L.; Duan, Y.; Shay, L.K. Tropical Cyclone Intensity Change from a Simple Ocean–Atmosphere Coupled Model. *J. Atmos. Sci.* **2001**, *58*, 154–172. [CrossRef]
46. Maneesha, K.; Murty, V.S.N.; Ravichandran, M.; Lee, T.; Yu, W.; McPhaden, M.J. Upper Ocean Variability in the Bay of Bengal during the Tropical Cyclones Nargis and Laila. *Prog. Oceanogr.* **2012**, *106*, 49–61. [CrossRef]
47. Mei, W.; Pasquero, C. Restratification of the Upper Ocean after the Passage of a Tropical Cyclone: A Numerical Study. *J. Phys. Oceanogr.* **2012**, *42*, 1377–1401. [CrossRef]
48. Wang, G.; Wu, L.; Johnson, N.C.; Ling, Z. Observed Three-Dimensional Structure of Ocean Cooling Induced by Pacific Tropical Cyclones. *Geophys. Res. Lett.* **2016**, *43*, 7632–7638. [CrossRef]
49. Wu, C.-R.; Chang, Y.-L.; Oey, L.-Y.; Chang, C.-W.J.; Hsin, Y.-C. Air-Sea Interaction between Tropical Cyclone Nari and Kuroshio. *Geophys. Res. Lett.* **2008**, *35*, L12605. [CrossRef]
50. Yu, J.; Zhang, H.; Wang, H.; Tian, D.; Li, J. Upper-Ocean Structure Variability in the Northwest Pacific Ocean in Response to Tropical Cyclones. *Front. Mar. Sci.* **2023**, *10*, 1245348. [CrossRef]
51. Balaguru, K.; Chang, P.; Saravanan, R.; Leung, L.R.; Xu, Z.; Li, M.; Hsieh, J.-S. Ocean Barrier Layers' Effect on Tropical Cyclone Intensification. *Proc. Natl. Acad. Sci. USA* **2012**, *109*, 14343–14347. [CrossRef] [PubMed]
52. Balaguru, K.; Foltz, G.R.; Leung, L.R.; Asaro, E.D.; Emanuel, K.A.; Liu, H.; Zedler, S.E. Dynamic Potential Intensity: An Improved Representation of the Ocean's Impact on Tropical Cyclones. *Geophys. Res. Lett.* **2015**, *42*, 6739–6746. [CrossRef]
53. Balaguru, K.; Foltz, G.R.; Leung, L.-Y.; Kaplan, J.; Xu, W.; Reul, N.; Chapron, B. Pronounced Impact of Salinity on Rapidly Intensifying Tropical Cyclones. *Bull. Am. Meteorol. Soc.* **2020**, *101*, E1497–E1511. [CrossRef]
54. Miles, T.N.; Coakley, S.J.; Engdahl, J.M.; Rudzin, J.E.; Tsei, S.; Glenn, S.M. Ocean Mixing during Hurricane Ida (2021): The Impact of a Freshwater Barrier Layer. *Front. Mar. Sci.* **2023**, *10*, 1224609. [CrossRef]
55. Neetu, S.; Lengaigne, M.; Vincent, E.M.; Vialard, J.; Madec, G.; Samson, G.; Ramesh Kumar, M.R.; Durand, F. Influence of Upper-Ocean Stratification on Tropical Cyclone-Induced Surface Cooling in the Bay of Bengal. *J. Geophys. Res. Oceans* **2012**, *117*, C12020. [CrossRef]
56. Vincent, E.M.; Lengaigne, M.; Vialard, J.; Madec, G.; Jourdain, N.C.; Masson, S. Assessing the Oceanic Control on the Amplitude of Sea Surface Cooling Induced by Tropical Cyclones. *J. Geophys. Res. Oceans* **2012**, *117*, C05023. [CrossRef]
57. Oey, L. A Simple Model of Sea-Surface Cooling under a Tropical Cyclone. *J. Mar. Sci. Eng.* **2023**, *11*, 397. [CrossRef]
58. Doong, D.-J.; Peng, J.-P.; Babanin, A.V. Field Investigations of Coastal Sea Surface Temperature Drop after Typhoon Passages. *Earth Syst. Sci. Data* **2019**, *11*, 323–340. [CrossRef]
59. Knapp, K.R.; Kruk, M.C.; Levinson, D.H.; Diamond, H.J.; Neumann, C.J. The International Best Track Archive for Climate Stewardship (IBTrACS): Unifying Tropical Cyclone Data. *Bull. Am. Meteorol. Soc.* **2010**, *91*, 363–376. [CrossRef]
60. Da, N.D.; Foltz, G.R.; Balaguru, K. A Satellite-Derived Upper-Ocean Stratification Data Set for the Tropical North Atlantic with Potential Applications for Hurricane Intensity Prediction. *J. Geophys. Res. Oceans* **2020**, *125*, e2019JC015980. [CrossRef]
61. Jean-Michel, L.; Eric, G.; Romain, B.-B.; Gilles, G.; Angélique, M.; Marie, D.; Clément, B.; Mathieu, H.; Olivier, L.G.; Charly, R.; et al. The Copernicus Global 1/12° Oceanic and Sea Ice GLORYS12 Reanalysis. *Front. Earth Sci.* **2021**, *9*, 698876. [CrossRef]
62. He, Y.; Lin, X.; Han, G.; Liu, Y.; Zhang, H. The Different Dynamic Influences of Typhoon Kalmaegi on Two Pre-Existing Anticyclonic Ocean Eddies. *Ocean Sci.* **2024**, *20*, 621–637. [CrossRef]
63. Yu, J.; Lv, H.; Tan, S.; Wang, Y. Tropical Cyclone-Induced Sea Surface Temperature Responses in the Northern Indian Ocean. *J. Mar. Sci. Eng.* **2023**, *11*, 2196. [CrossRef]
64. Kara, A.B.; Rochford, P.A.; Hurlburt, H.E. An Optimal Definition for Ocean Mixed Layer Depth. *J. Geophys. Res. Oceans* **2000**, *105*, 16803–16821. [CrossRef]
65. Fiedler, P.C. Comparison of Objective Descriptions of the Thermocline. *Limnol. Oceanogr. Methods* **2010**, *8*, 313–325. [CrossRef]
66. Jin, M.; Zhao, Z.; Wu, R.; Zhu, P. Latitudinal and Seasonal Variations in Tropical Cyclone-Induced Ocean Surface Cooling in the Tropical Western North Pacific. *J. Meteorol. Res.* **2023**, *37*, 790–801. [CrossRef]

Disclaimer/Publisher's Note: The statements, opinions and data contained in all publications are solely those of the individual author(s) and contributor(s) and not of MDPI and/or the editor(s). MDPI and/or the editor(s) disclaim responsibility for any injury to people or property resulting from any ideas, methods, instructions or products referred to in the content.